Computing focused beam transmissions of photonic crystals using angular spectrum field synthesis

Siemons, Marijn; Kohlhaas, Ralf

DOI
10.1364/OE.553298

Publication date
2025

Document Version
Final published version

Published in
Optics Express

Research Article | Vol. 33, No. 6 / 24 Mar 2025 / Optics Express 12444
Optics EXPRESS

Computing focused beam transmissions of photonic crystals using angular spectrum field synthesis

MARIJN SIEMONS[1] AND RALF KOHLHAAS[1,2,*]

[1]SRON, Netherlands Institute for Space Research, 2333 CA Leiden, The Netherlands
[2]Department of Precision and Microsystems Engineering, Delft University of Technology, 2628 CD Delft, The Netherlands
[*]r.kohlhaas@tudelft.nl

Abstract: Recently novel types of imaging spectrometers have been successfully demonstrated, where photonic crystals filters are placed onto a detector. For focused beams, it is however unclear how numerical aperture (NA), aperture shape and aberrations affect the transmission of these filters and there is currently no established and computational efficient method to assess this. In this work we present an angular spectrum method to reconstitute focused beam fields and transmissions based on plane wave simulations. Once these plane wave simulations have been performed, the transmission of arbitrary pupils, aberrations and NA can be directly computed. We investigate the accuracy of this method by comparing the synthesized transmission and Poynting vectors with a fully simulated focused Gaussian beam. These results show that an angular sampling between 0.5° and 0.8° is required to achieve an accurate result depending on the mesh sampling of the simulation. Lastly, we demonstrate how this method can be used to investigate the effect of the pupil shape and aberrations on the transmission profiles. This analysis enables the identification of spectral regions which are sensitive to the instrument design but also regions which appear robust. We believe that the method described in this work can provide scientists and optical engineers a tool to perform detailed performance studies on these promising new instruments.

1. Introduction

On-chip spectrometers [1–8] are a new type of imaging spectrometer where photonic crystals (PC) slabs are placed onto a detector which act as optical filters. These filters allow to reconstruct the spectrum using (compressive sensing) reconstruction techniques [9–12] or directly infer other information such as gas concentrations [1,13,14]. In this concept, traditional dispersion optics (i.e., gratings and prisms) are no longer needed, due to the strong dispersive resonances in the photonic crystal. One particular interesting application is in space instruments, such as remote sensing [15], where the latter size is often a major cost driver. In remote sensing, a typical application is an imaging spectrometer in a push-broom configuration [16]. This type of instrument consists of a telescope and spectrometer, of which the latter is the largest contributing factor to the size of the instrument. In the novel photonic crystal enabled spectrometers, the spectrometer is reduced to a flat optical component, which reduces the size of the instrument considerably.

Typically, PC slab transmissions are computed with plane wave excitation, often using Finite Difference Time Domain (FDTD) simulations [17] or Rigorous Couple Wave Analysis (RCWA) [18]. However, in a photonic crystal enabled imaging spectrometer, light is focused onto the detector chip, which deviates from plane wave simulations. Therefore, to assess the performance

#553298 https://doi.org/10.1364/OE.553298
Journal © 2025 Received 17 Dec 2024; revised 27 Jan 2025; accepted 29 Jan 2025; published 10 Mar 2025

Optics EXPRESS

of these concepts the photonic crystals filter responses for a focused beam are needed. Moreover, the numerical aperture (NA) or F-number of the imaging system is a major performance driver in any optical instrument. In traditional optical instruments, faster optics allow for a larger etendue (more light collection) and higher (spectral) resolution, typically at the cost of optical aberrations and system complexity. This trade-off has been extensively studied for optical instrument design and is well understood [19]. Since the spectral performance of the photonic crystals is as well affected by the NA, aperture shape and optical aberrations, these new types of compressive sensing imaging spectrometers raise an additional consideration to this trade-off.

In order to investigate this trade-off, numerous focused beam simulations have to be performed, including many optical aberration configurations. FDTD is required for a focused beam simulation, which is computationally expensive in this configuration. The physical simulation domain should compass the full Point Spread Function (PSF) which can span 10-100 μm, depending on the application and wavelength. The 3D simulation domain should ideally be highly sampled (>16 points per wavelength, ppw) [20], which leads to long computation times (>50h for a single simulation) and large memory demands.

To complicate things further, one major advantage of this new spectrometer concept is that the photonic crystals filters can be chosen such that they optimize the information measured for the intended purpose of the device [21,22]. Typically, many different filters have to be simulated and a filter library with thousands of filters is created, after which a selection is made. However, filters which might perform well under plane wave conditions, might perform poorly in the focused beam condition. Therefore, the performance trade-off of the photonic crystal filters should be made with the complete focused beam transmission library. This poses additional constraints on the focused beam simulations. Not only do they have to be performed for different NA's, pupil shapes and aberration conditions, the assessment has to be performed for many thousands of filters which would take many years of computation time. Therefore direct FDTD simulations of focused beams are not a feasible path for such an optimization.

An alternative way to compute the transmission of a focused beam is to synthesize the electric and magnetic field of the focused beam from plane waves [23,24], also known as the angular spectrum method [25]. Since the computational demand is much smaller for a single unit cell, this simulation can be easily paralyzed on clusters or servers. Moreover, the major advantage of this approach is that once the simulation for all angles has been performed, the transmission of the photonic crystal for any pupil, NA and aberration condition can be directly computed. A previous method proposed by Xu et al. [26] claims that the transmission of a focused beam of a PC slab can be computed as the (weighted) integral of individual plane wave transmission profiles for a range of 1D angles. We would argue that in general this approach is incorrect for two reasons. First, the pupil should be integrated in 2D, taking into account the different responses depending on the azimuthal angle in the pupil. Secondly, the electric and magnetic fields should be integrated independently first over the pupil before computing the flux and overall transmission [24].

In this work we describe a methodology how the angular spectrum method can be used to synthesize the electric and magnetic fields using plane wave simulations of a single unit cell with different incidence angles, see Fig. 1(b). The reconstituted fields can then be used to compute the flux and transmission of the PC slab. We investigate the trade off between the achieved accuracy and the angular sampling by comparing the synthesized transmission with a focused Gaussian beam simulation. We show how photonic crystal symmetry, if present, can be correctly applied to reduce the number of required simulations and several implementation details which should be taken into account. Lastly, we demonstrate how this approach can be used to compute and investigate the transmission for photonic crystals for different NA's and pupil functions and how optical aberrations can impact the transmission profile of the photonic crystal.

Optics EXPRESS

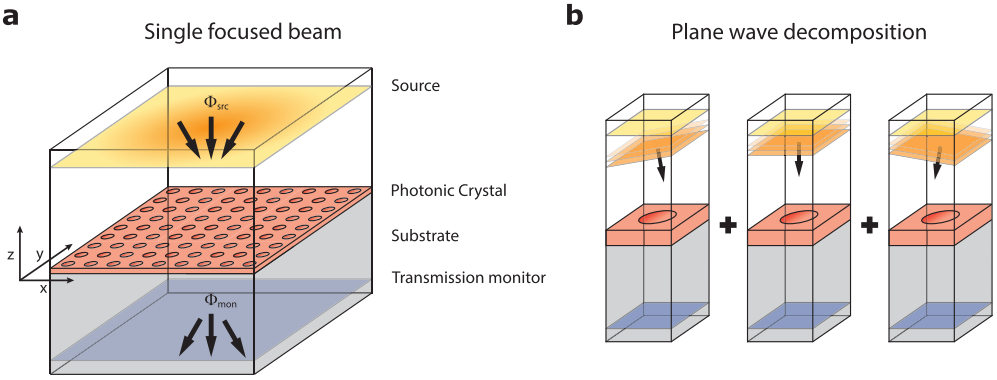

Fig. 1. a) Illustration of a single focused beam FDTD simulation with a Gaussian source. b) Illustration of the plane wave decomposition. The focused beam of (a) can be described as a linear combination of angled plane wave simulations of a single unit cell.

2. Theory

Consider a 2D photonic crystal slab spanning the plane $\vec{x} = (x, y)$ consisting of a substrate with a thin film of amorphous silicon (aSi) where the photonic crystal is etched into (Fig. 1). The source plane is located at the z-plane at position h and the transmission monitor is located in the z-plane at position $-h$. The transmission of the photonic crystal T is given by the ratio of the electromagnetic flux Φ through the source plane and transmission monitor

$$T = \frac{\Phi_{\text{mon}}}{\Phi_{\text{src}}}. \tag{1}$$

The time averaged electromagnetic flux is given by [27]

$$\Phi = -\frac{1}{2}\int_{\vec{x}} \Re\left[S_z\left(\vec{x}\right)\right] d\vec{x} = -\frac{1}{2}\int_{\vec{x}} \Re\left[\vec{E}\times\vec{H}^{\dagger}\right]_z d\vec{x} \tag{2}$$

with S_z the z-component of the instantaneous Poynting vector and $\vec{E}$ and $\vec{H}$ the electric and magnetic field respectively of the focused beam. Using plane wave decomposition, the $\vec{E}$- and $\vec{H}$-field of the focused beam can be described as a linear combination of plane waves with appropriate phase and amplitude

$$\vec{E}\left(\vec{x}\right) = \int_{\vec{\rho}} P(\vec{\rho})\vec{E}^{\text{pw}}\left(\vec{x},\vec{\rho}\right)\exp\left[-i\left(k\vec{\rho}\cdot\vec{x}+k_z h\right)\right] d\vec{\rho} \tag{3}$$

with $\vec{\rho} = [n\sin(\theta\cos(\phi)), n\sin(\theta\sin(\phi))]$ the pupil coordinate in Cartesian coordinates, n the refractive index, and θ and ϕ the incidence angle and azimuthal angle in cylindrical coordinates respectively, see Fig. 2. $\vec{E}^{\text{pw}}$ denotes the electric field for the plane wave excitation, $k = 2\pi/\lambda$ the angular wave number, $k_z = 2\pi\sqrt{n^2 - \text{NA}^2/\rho^2}/\lambda$ the z-component of the wave vector and $P(\vec{\rho})$ is the pupil function, which is given by

$$P(\vec{\rho}) = A(\vec{\rho})\exp\left[-ikW(\vec{\rho})\right], \tag{4}$$

where $A(\vec{\rho})$ is the aperture function and $W(\vec{\rho})$ the optical aberration. Similarly to Eq. (3), the magnetic field is given by

$$\vec{H}\left(\vec{x}\right) = \int_{\vec{\rho}'} P(\vec{\rho}')\vec{H}^{\text{pw}}\left(\vec{x},\vec{\rho}'\right)\exp\left[-i\left(k\vec{\rho}'\cdot\vec{x}+k_z h\right)\right] d\vec{\rho}' \tag{5}$$

Optics EXPRESS

with $\vec{H}^{\mathrm{pw}}$ the magnetic field in the case of plane-wave excitation. Here $\vec{\rho}'$ indicates that Eq. (3) and (5) are two distinct pupil integrals. The E- and H-fields at both the source plane and monitor plane are synthesized and the transmission is computed according Eq. (1) and (2).

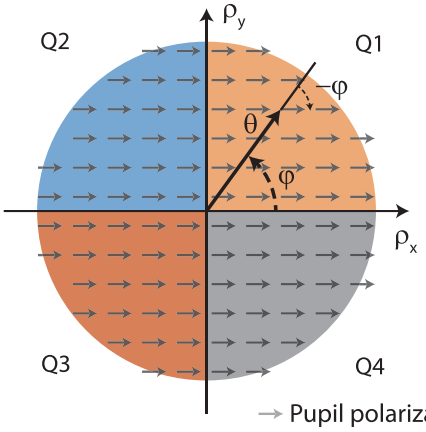

Fig. 2. Pupil coordinate system with quadrants. θ is the incident angle and ϕ the azimuthal angle. The colors indicate the different quadrant of the pupil (Q1-Q4). The grey arrows indicate the polarization across the pupil. To achieve a linear polarized pupil, the polarization should be rotated by $-\phi$ in the FDTD plane wave simulation.

3. Photonic crystal simulations

We performed two types of photonic crystal simulations, a large focused beam simulation and plane wave simulations with a single unit cell. Both are simulated using Finite-Difference Time-Domain (FDTD) in Lumerical (2023, Ansys), see Fig. 1.

The simulation domain consists of a of quartz substrate with a 415 nm layer of amorphous silicon (aSi) on top. The photonic crystal is etched into the aSi layer and consists of circles with with a periodicity of a = 1 µm and a radius r = 250 nm (r/a = 0.25). The wavelength range is chosen to be of [1.5–1.8] µm in 1 nm steps as the photonic crystal exhibits several interesting features in this range. To compare the transmission profiles we choose an maximum excitation angle of θ_{max} = 5°, corresponding to an NA of 0.09 and F-number 5.7. All simulations are performed on a workstation (Intel Xeon Silver 4108) with 380 GB memory space.

3.1. Focused beam simulation

In the case of the focused Gaussian beam, the simulation domain spans an area of 51 µm × 51 µm, which is sufficiently large to capture the $1/e^4$ intensity threshold (± 24 µm). The simulation domains spans [-2.5–3.0] µm in the z-direction and the source plane and transmission monitor are placed at 2.5 µm and -2 µm respectively. For all boundaries a Perfectly Matched Layer (PML) is applied of type 2 (stabilized) and the mesh accuracy is set to 3 (14 points per wavelength, ppw), resulting in spatial sampling of roughly 30 nm. All objects extend through the PML layer except the etching layer. It was found that this highly dispersive feature leads to diverging simulations when extended through the PML boundary. Therefore the aSi-layer and substrate were extended, but not the photonic crystal pattern. This resulted in converging simulations.

3.2. Plane wave simulations

For the plane-wave simulations, the simulation domain consist of a single unit cell, in this case 1 µm × 1 µm. The source and transmission monitor are placed at the identical z-positions as the

Optics EXPRESS

focused beam simulation. For the x- and y-boundary, a Bloch boundary condition is applied to account for the angled plane wave. For the z-boundary, a PML applied of type 2 (stabilized) and the mesh accuracy is set to 3 (14 ppw).

To achieve the linear polarization identical to the focused beam simulation, care should be taken to rotate the polarization of the source accordingly. For an angle of incidence θ and azimuthal angle ϕ, the polarization angle of the source should be rotated by $-\phi$ to achieve a linear polarized pupil, matching the focused beam simulation, see Fig. 2.

Once the FDTD simulations are performed, the individual electric and magnetic fields are stitched together to form the full electric and magnetic field of the focused beam. The output E- and H-field of the FDTD simulations already contain the local phase ramp of the angled plane wave, i.e. $\exp\left[-ik\vec{\rho}\cdot\vec{x}'\right]$, where $\vec{x}'$ denotes the local simulation grid. Therefore only the additional phase offset induced by the stitching has to be added. The electric field $\vec{E}^{l,m}$ and magnetic field $\vec{H}^{l,m}$ at unit cell location index (l, m) are then given by

$$\vec{E}^{l,m}\left(\vec{x}\right) = \int_{\vec{\rho}} P(\vec{\rho})\vec{E}^{\text{sim}}\left(\vec{x}', \vec{\rho}\right) \exp\left[-ika\left(l\rho_x + m\rho_y\right)\right] d\vec{\rho} \tag{6}$$

and

$$\vec{H}^{l,m}\left(\vec{x}\right) = \int_{\vec{\rho}} P(\vec{\rho})\vec{H}^{\text{sim}}\left(\vec{x}', \vec{\rho}\right) \exp\left[-ika\left(l\rho_x + m\rho_y\right)\right] d\vec{\rho} \tag{7}$$

with $\vec{E}^{\text{sim}}$ and $\vec{H}^{\text{sim}}$ the simulated FDTD electric and magnetic fields with local grid coordinates $\vec{x}'$ and a the lattice constant.

3.3. Pupil sampling

The pupil is sampled in a hexapolar fashion, commonly used in geometric optical transfer function sampling and ray tracing [28]. For hexapolar sampling, the pupil is sampled in a grid with node coordinates $(\theta_j, \phi_{i,j})$, with $\theta_j = j\theta_{\max}/n_{\text{rings}}, \ldots, \theta_{\max}$ and $\phi_{i,j} = i\pi/(3nj), \ldots, 2\pi$, where is n_{rings} the number of rings. We performed pupil samplings at 6 different densities $n_{\text{rings}} = [30, 15, 10, 6, 3, 2]$, where each sampling is a subset of $n_{\text{rings}} = 30$, see Fig. 3. These densities result in an angular sampling of $\Delta\theta = 0.16°$, $0.33°$, $0.5°$, $0.83°$, $1.66°$ and $2.5°$ respectively.

Due to the photonic crystal symmetry, only 1 quadrant of the pupil has to be simulated, reducing simulation time. To retrieve the electric and magnetic fields of the other quadrants of the pupil the following modifications to the E- and H-fields have to be made:

1. for $\pi/2 < \phi \leq \pi$ (Quadrant 2):
   - Flip E- and H-field in the x-direction.
   - $\vec{E}^{Q2} = \begin{bmatrix} E_x^{Q1} \\ -E_y^{Q1} \\ -E_z^{Q1} \end{bmatrix}$ and $\vec{H}^{Q2} = \begin{bmatrix} -H_x^{Q1} \\ H_y^{Q1} \\ H_z^{Q1} \end{bmatrix}$
2. for $\pi < \phi \leq 3\pi/2$ (Quadrant 3):
   - Flip E- and H-field in the x- and y-direction.
   - $\vec{E}^{Q3} = \begin{bmatrix} E_x^{Q1} \\ E_y^{Q1} \\ -E_z^{Q1} \end{bmatrix}$ and $\vec{H}^{Q3} = \begin{bmatrix} H_x^{Q1} \\ H_y^{Q1} \\ -H_z^{Q1} \end{bmatrix}$

Optics EXPRESS

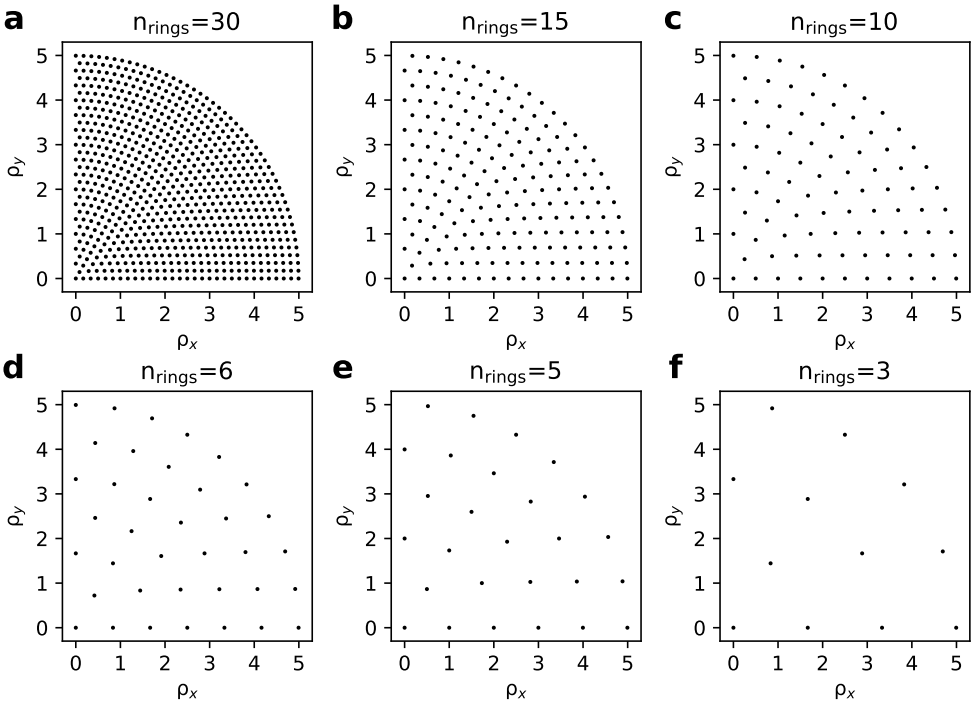

Fig. 3. Hexapolar pupil sampling for 6 chosen densities. The total number of pupil samples for each quadrant is 721, 192, 91, 37, 27 and 12 for $n_{\text{rings}} = 30, 15, 10, 6, 5$ and 3 respectively.

3. for $3\pi/2 < \phi \leq 2\pi$ (Quadrant 4):
   - Flip E- and H-field in the y-direction.
   - $\vec{E}^{Q4} = \begin{bmatrix} E_x^{Q1} \\ -E_y^{Q1} \\ E_z^{Q1} \end{bmatrix}$ and $\vec{H}^{Q4} = \begin{bmatrix} -H_x^{Q1} \\ H_y^{Q1} \\ -H_z^{Q1} \end{bmatrix}$

The full angular spectrum field synthesis workflow is therefore as follows. First FDTD simulations are performed for a single PC unit cell for a range of different angles of a single pupil quadrant. The fields for the 3 other quadrants are calculated using the above-mentioned symmetry. Then the pupil integrals (Eq. (6) and (7)) are computed for each unit cell location and the fields are stitched for both the fields at the source plane and the monitor plane. Lastly, the flux is computed by integrating the fields over de xy-plane (Eq. (2)) and the transmission is found as the ratio between the monitor and source plane (Eq. (1)).

3.4. Pupil shapes

We tested the impact on the transmission profile for several different pupil shapes, as shown Fig. 4. The pupil shapes consist of a Gaussian apodization, a top hat and an annulus, see Fig. 4. The top hat profile will result in an Airy disk focus and has a transmission of 1 for $\theta \leq 5°$ and 0 otherwise. The annulus is a common optical design for telescopes and for this design has a transmission of 1 for $2° \leq \theta \leq 5°$ and 0 otherwise. The Gaussian apodization will result in a Gaussian beam and is given by $P(\theta) = A \exp[-\sin(\theta)^2/\sigma^2]$ with $\sigma = \sin(2.5°)$ and A a normalization factor. With this amplitude apodization, the intensity of the beam is $1/e^4$ at $\theta = 5°$.

Optics EXPRESS

These pupil shapes are of interest for the following reasons. First, the Airy disk is the most commonly used PSF in instruments, but electromagnetically not trivial. The phase of the electric and magnetic field of Airy rings oscillate 180°, thereby affecting the resonances in the photonic crystal, see Fig. 4(b)&(c). In contrast, the Gaussian beam excitation is less spatially constraint and maintains the phase of the excitation across the whole PSF. Lastly, the PSF with an annulus pupil is similar to an Airy disk but contains more pronounced interference rings. These pupil shapes therefore provide interesting information how these different excitations, each with specific amplitude and phase profiles, affect the transmission of the PC slab.

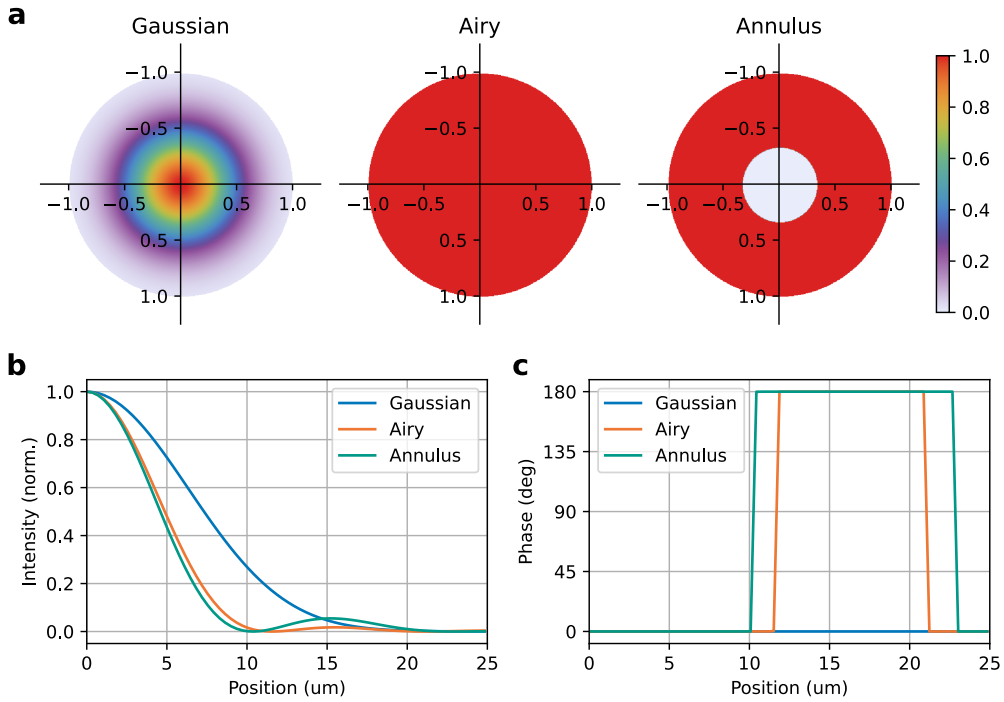

Fig. 4. (a)-(c) Pupil apodization used in this work: Gaussian, Airy and and annulus, shown here in normalized pupil coordinates. (b),(c) The associated intensity distributions (b) and phase (c) of the three different pupil apodizations.

3.5. Aberrations

The pupil function in Eq. (3) can contain optical aberrations $W(\vec{\rho})$. Here the optical aberration is described using a combination of Zernike modes Z_i with amplitude A_i

$$W(\vec{\rho}) = \sum_i A_i Z_i(\vec{\rho}) \tag{8}$$

with i the Noll index. The Zernike modes are RMS normalized such that the total RMS aberration level is $W_{\text{rms}} = \sqrt{\sum_i A_i^2}$.

We explore the effect of three common optical aberrations: astigmatism, coma and primary spherical aberration with W_{rms} levels ranging from 0 to 400 mλ. For reference, an optical system is presumed to be diffraction limited when $W_{\text{rms}} \leq 72$ mλ (Maréchal criterion).

Optics EXPRESS

4. Results

4.1. Transmission and field accuracy

Before we compare the transmission and Poynting vector of the fully simulated focused beam and field synthesized beam, it is worthwhile to investigate the transmission profiles of the PC slab for angled plane waves. Figure 5 shows the transmission profile as function of angle for P- and S-polarization. These correspond to the $\phi = 0°$ and $\phi = 90°$ case of the plane wave simulations. The photonic crystal slab exhibits a sharp resonance feature at 1518 nm and a broader reflection feature around 1700 nm. The sharp spectral feature splits into two separate resonances, depending on the polarization state, while the broad feature appears to be relatively insensitive to the angle of incidence and polarization. Based on this assessment we expect the transmission of the focused beam to maintain the broad reflection feature, but no sharp feature at 1518 nm as it will be smooth out. Fig. 6(a)-c shows the transmission derived from the fully simulated focused beam and the field synthesized beam, alongside the transmission for the orthogonal plane wave. As expected, the focused beam transmission also shows the broad reflection feature but not the resonance feature at 1518 nm. Instead, two different feature arise at 1508 and 1521 nm, which are present in both the fully simulated as well as the synthesized focused beam. In general, the transmission of the focused beam simulation and the field synthesized beam align very well. Both transmission profiles include the two resonance features and in overall the RMS difference between two transmission profiles is 2%.

Despite the sharp transmission feature in the plane wave simulations, the synthesized beam transmission appears to be smooth for high pupil samples (see Fig. 6(d)-f). With fewer pupil samples, the transmission profile becomes less smooth with more erratic features around 1500–1530 nm, although the overall transmission does not change with fewer pupil samples.

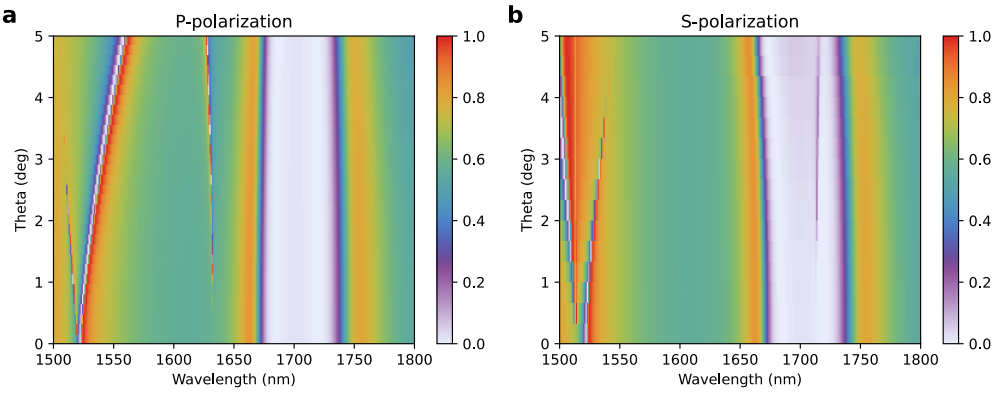

Fig. 5. Transmission profiles of the photonic crystal slab for plane wave excitation for P-polarization (a) and S-polarization (b).

To quantify the difference between the fully simulated and synthesized beam we computed the RMS difference between the transmission profiles for two different mesh accuracy settings, as shown in Fig. 7. This reveals that for finer pupil sampling the difference decreases and the fidelity of the field synthesis beam improves. However, the best RMS difference which can be achieved seems to depend strongly on the general mesh accuracy of the simulations. For mesh accuracy #2, the best achievable RMS difference is 3.8%, while for mesh accuracy #3 this is 2%.

This indicates that the main driver for the difference between the fully simulated and synthesized beam is the mesh accuracy of the simulation itself. In other words, at a certain pupil sampling, the accuracy of the field synthesized beam and the fully simulated beam is limited by the mesh sampling and not the pupil sampling. Therefore, the observed difference in transmission profiles

Optics EXPRESS

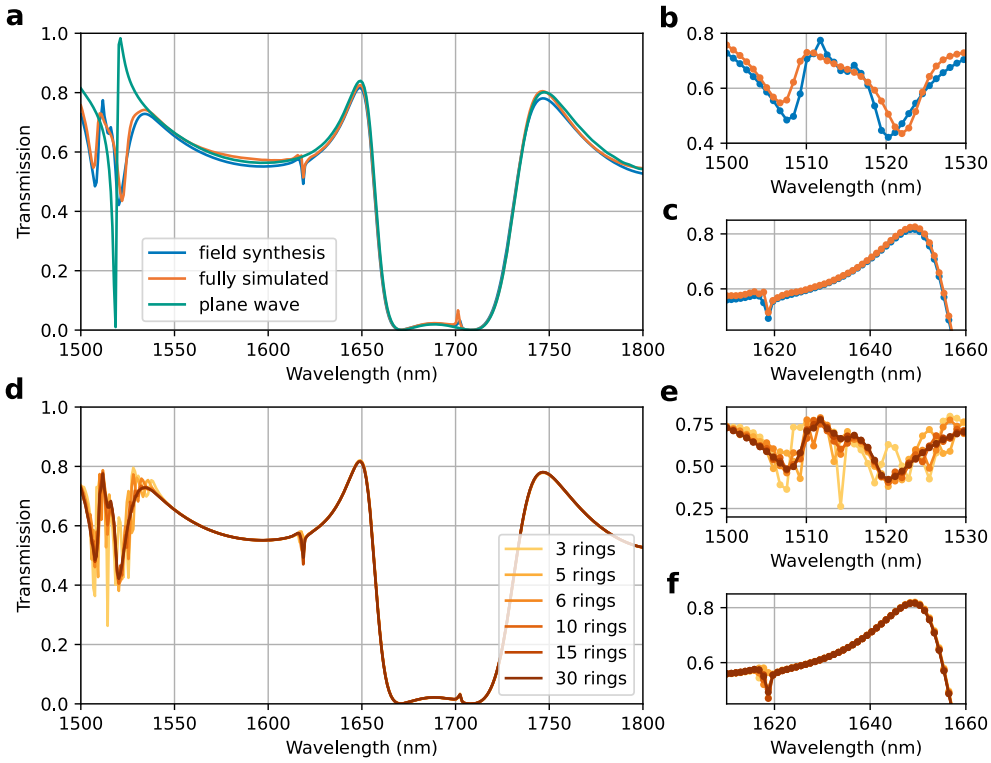

Fig. 6. (a) Transmission profile for the fully simulated focused beam, the field synthesized beam with $n_{\text{rings}} = 30$ pupil sampling and plane wave. (b) and (c) Zooms of (a). (d) Transmission profile of the synthesized beam for different pupil samplings. (e) and (f) Zooms of (d).

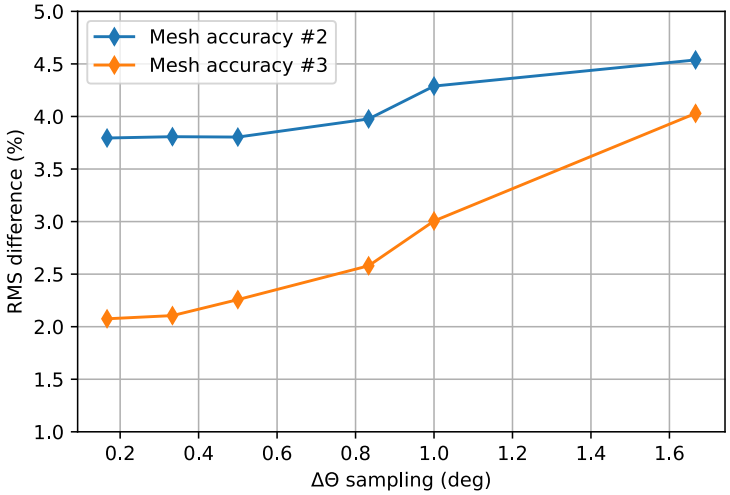

Fig. 7. RMS difference between the fully simulated and synthesized beam as function of pupil sampling for mesh accuracy #2 (10 ppw) and #3 (14 ppw).

Optics EXPRESS

lies in the meshing difference between the two simulations, as mesh staircasing can be a main source of error in FDTD [29–31].

These results reveal computationally cost-effective pupil samplings, relative to the overall accuracy of the simulation set by the meshing sampling. Good pupil samplings appear to be at 0.8° sampling for mesh accuracy #2 and 0.5° sampling for mesh accuracy #3. For this mesh accuracy and pupil sampling, the 91 plane wave simulations required for the field synthesis took 42h to compute, compared to the 70h of the fully simulated beam. The field synthesize method is therefore not only more versatile but is faster to compute in order to reach a similar level of accuracy.

Figure 8 shows the Poynting vector recorded by the fully simulated focused beam and the synthesized Poynting vector for 2 different wavelengths (λ = 1800 nm and λ = 1657 nm). For 1800 nm, the transmission difference between the fully simulated and synthesized beam is 2% (54% vs 52% resp.) and the difference in Poynting vectors appears to be smooth with little electromagnetic interaction inside the PC slab. Surprisingly, for 1657 nm the Poynting vector of the field synthesized beam features more pronounced oscillations inside the PC slab with local relative differences larger than 20%. Nonetheless, the overall flux is very similar between the two simulations (2.2% vs 2.3%). These examples illustrate two cases. One case where the overall transmission deviates relatively much, but the structure of the Poynting vector matches well and a case where the overall transmission matches well, but the Poynting vector deviates more strongly. We attribute these differences to the meshing accuracy and expect these differences to converge with higher samplings at the expense of computational time.

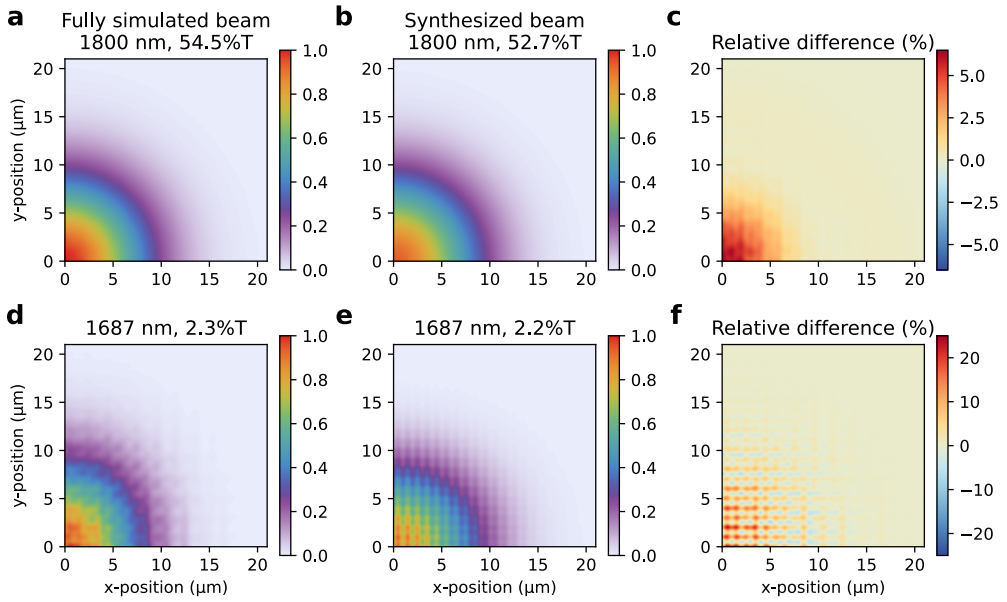

Fig. 8. Poynting vector of the fully simulated beam (a) and synthesized beam (b) for λ = 1800 nm. (c) The relative difference between the (a) and (b). (d)-(f). Similar as (a)-(c) but for λ = 1687 nm.

4.2. *Pupil shape impact*

With the effectiveness and fidelity of the field synthesized transmission established, we next investigated the effect of different pupils on the transmission profile, as shown in Fig. 9. The Poynting vector, (Fig. 9(a)-c), is more confined for the airy and annulus pupil as expected and the

Optics EXPRESS

airy ring is visible and more pronounced for the annulus pupil. Interestingly, the transmission profiles of the airy disk and annulus deviate substantially from the Gaussian beam transmission between 1500 and 1550 nm. The peak at 1520 nm of the Gaussian beam disappears for the Airy and annulus pupil, but the peak at 1508 nm remains. This brief investigation shows how the pupil shape can alter the transmission of PC filters, depending on the type of resonance features.

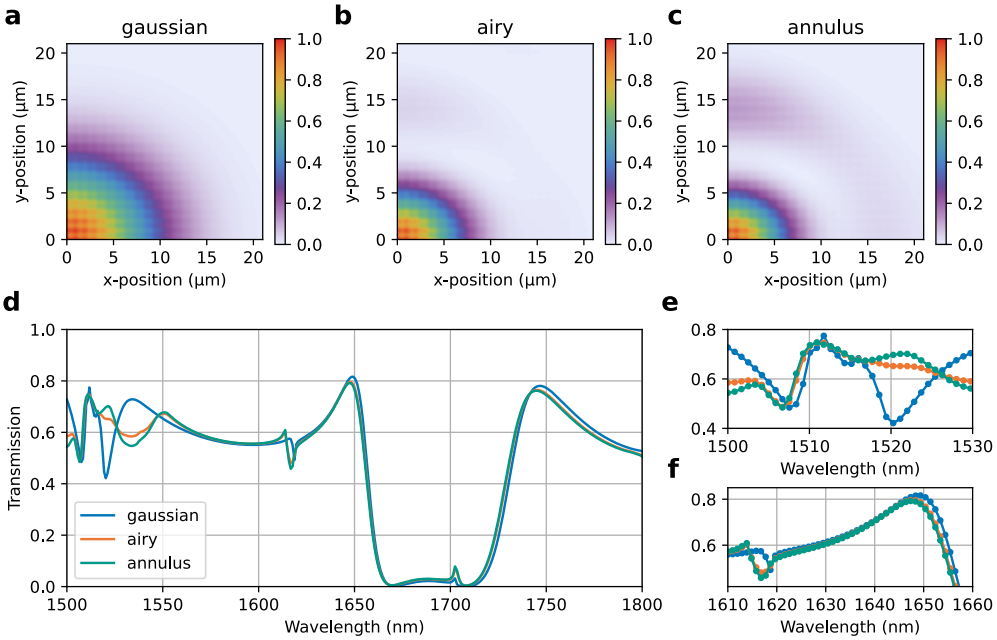

Fig. 9. (a)-(c) Synthesized Poynting vector for Gaussian (a), Airy (b) and annulus (c) pupil apodization for $\lambda = 1687$ nm. (d) Transmission profiles of the three pupil apodizations. (e) and (f) Zooms of (d).

4.3. *Aberration impact*

Lastly, we assessed the impact of optical aberrations on the transmission profile of the PC slab. For this we selected the Airy beam as is it the most commonly used pupil and $n_{\text{rings}} = 15$ pupil sampling ($\Delta\theta = 0.33°$). In this case the size of field synthesized beams are increased to ±42 um, to fully capture the aberrated PSF. Figure 10 shows the synthesized PSFs for different aberrations and the associated transmission profiles. This analysis reveals that the effect of astigmatism is small on the transmission profile, whereas both coma and spherical do have an impact on the transmission profile but affect different spectral regions. Coma appears to reduce the transmission at 1530 nm whereas spherical aberration increases the transmission around 1540 nm. Furthermore, the transmission profiles shown in Fig. 10(d)-f appear more erratic and noisier compared to the transmission profile computed using 30 rings (Fig. 9(d)). This indicates that the Airy disk, in combination with aberrations is more sensitive to the pupil sampling and suggests that a higher pupil sampling might be preferential for these cases. Figure 11 shows the RMS difference in transmission as function of aberration level for three aberrations for 2 wavelength bands [1500 – 1800] nm and [1500 –1580] nm. It appears that the transmission of this PC slab is relatively robust against astigmatism, but sensitive to spherical aberration. Furthermore, the transmission is generally more robust against aberrations in the [1580 –1800] nm band.

We believe that this type of analysis will be useful in tolerance studies. Optical design software can produce thousands of aberration configurations, based on the mechanical tolerances of the

Optics EXPRESS

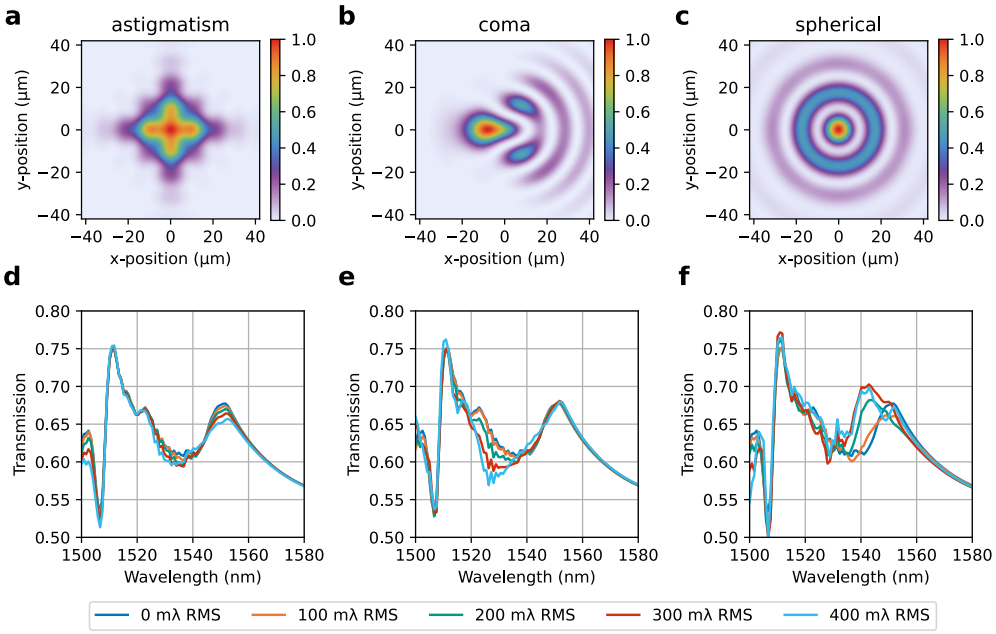

Fig. 10. (a)-(c) Field synthesized Poynting vector for astigmatism (a), coma (b) and spherical (c) aberration with an aberration level of 200 mλ. (d)-(f) Transmission profiles for astigmatism (d), coma (e) and spherical (f) for different aberration levels.

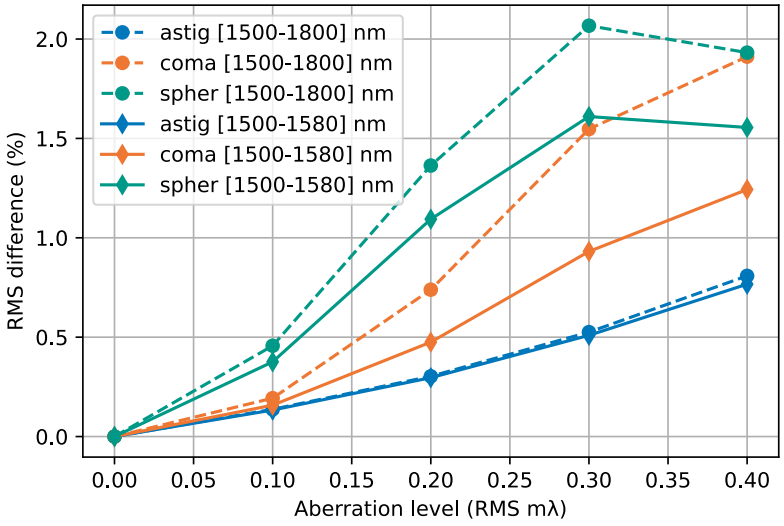

Fig. 11. RMS difference in transmission as function of aberration level for astigmatism, coma and spherical aberration and two different wavelength ranges

Optics EXPRESS

optical components. These aberration configurations can be used to compute the associated transmission profiles and in turn to assess the instrument performance, closing the performance optimization loop. Another use case would be to assess the impact of aberrations induced by thermal deformations of the instrument, generally experienced by flight instruments, or misalignment caused by settling effects of optical components after launch. Structural Thermal Optical Performance (STOP) analysis together with the angular spectrum field synthesis can be used for end-to-end performance modeling of the full optical instrument. These proposed workflows highlight the need for a cost-effective computationally implementation as presented in this work.

5. Conclusion

Novel photonic crystal enabled spectrometers introduce an additional performance trade-off in the form of the photonic crystal transmission; unique to this type of instrument. The photonic crystal transmission, and by that the spectral reconstruction accuracy, has to be traded against signal-to-noise, optical performance and imaging resolution. In this work we provide a tool how to efficiently analyze and assess this trade-off. We show that, using angular spectrum field synthesis, it is possible to compute transmission profiles for many different instrument configurations, NA's and aberration levels in a computationally efficient manor.

It appears that, for the photonic crystal slab used in this study, an angular sampling of 0.5° is required to achieve an accurate result for a mesh accuracy #3 (14 points per wavelength) and an angular sampling of 0.8° for mesh accuracy #2 (10 points per wavelength). Depending on the type of resonances present in the PC slab in the wavelength band, a finer sampling might be preferential in the case for an Airy or annulus pupil shape.

The presented method can be used to efficiently assess the impact of the pupil shape and optical aberrations on the transmission. For the PC slab under study we find that the transmission is quite strongly dependent on the pupil shape, for specific sharp resonances, whereas the other spectrally broader feature appears more resilient. This behavior might differ for different photonic crystal filters or depend on the type of electromagnetic resonances present in the filter. However, small differences in transmission can already result in performance degradation in applications such as computational spectroscopy [11] or gas measuring devices [2,14] where the exact transmission profile directly influences the performance of the instrument.

We furthermore show that for this PC slab design optical aberrations affect different regions of the transmission profile and described how such an assessment can be used in tolerance studies and end-to-end performance modeling. Additionally, this method can be used for polarization sensitive PC slabs and other nanophotonic filters such as metasurface filters [32,33]. In case of polarization sensitive metasurface filters such as in [34], the workflow remains identical, except in that case two pupil quadrants have to be simulated for two pupil polarizations.

The angular spectrum field synthesis method presented in this work is not only more versatile, allowing for different pupils, aberrations and NA's, the required plane wave simulations to reach a similar accuracy as the fully simulated beam are almost twice as fast to compute compared to a single configuration of a fully simulated focused beam. Therefore we believe that the methodology presented here is therefore a useful tool to design these highly specialized optical instruments.

Acknowledgments. The authors would like to thank Aurèle Adam, René Berlich, David Doelman for useful discussion and feedback.

Disclosures. The authors declare no conflicts of interest.

Data availability. All data and code underlying the results presented in this paper are made publicly available at Zenodo [35]. Additionally, all code can also be found at the publicly available Github repository pc-field-synthesis [36] and we welcome contributions.

Optics EXPRESS

References

1. A. Tittl, A. Leitis, M. Liu, *et al.*, "Imaging-based molecular barcoding with pixelated dielectric metasurfaces," Science **360**(6393), 1105–1109 (2018).
2. J. Meng, J. J. Cadusch, and K. B. Crozier, "Detector-only spectrometer based on structurally colored silicon nanowires and a reconstruction algorithm," Nano Lett. **20**(1), 320–328 (2020).
3. C. Chen, X. Li, G. Yang, *et al.*, "Computational hyperspectral devices based on quasi-random metasurface supercells," Nanoscale **15**(19), 8854–8862 (2023).
4. Z. Wang, S. Yi, A. Chen, *et al.*, "Single-shot on-chip spectral sensors based on photonic crystal slabs," Nat. Commun. **10**(1), 1020 (2019).
5. J. Xiong, X. Cai, K. Cui, *et al.*, "Dynamic brain spectrum acquired by a real-time ultraspectral imaging chip with reconfigurable metasurfaces," Optica **9**(5), 461–468 (2022).
6. J. Yang, K. Cui, X. Cai, *et al.*, "Ultraspectral imaging based on metasurfaces with freeform shaped meta-atoms," Laser Photonics Rev. **16**(7), 2100663 (2022).
7. G. Cai, Y. Li, Y. Zhang, *et al.*, "Compact angle-resolved metasurface spectrometer," Nat. Mater. **23**(1), 71–78 (2024).
8. J. Yang, K. Cui, Y. Huang, *et al.*, "Deep?learning based on?chip rapid spectral imaging with high spatial resolution," Chip **2**(2), 100045 (2023).
9. Z. Wang and Z. Yu, "Spectral analysis based on compressive sensing in nanophotonic structures," Opt. Express **22**(21), 25608–25614 (2014).
10. C.-C. Chang and H.-N. Lee, "On the estimation of target spectrum for filter-array based spectrometers," Opt. Express **16**(2), 1056–1061 (2008).
11. Z. Yang, T. Albrow-Owen, W. Cai, *et al.*, "Miniaturization of optical spectrometers," Science **371**(6528), eabe0722 (2021).
12. U. Kurokawa, B. I. Choi, and C.-C. Chang, "Filter-based miniature spectrometers: Spectrum reconstruction using adaptive regularization," IEEE Sens. J. **11**(7), 1556–1563 (2011).
13. J. Meng, S. Balendhran, Y. Sabri, *et al.*, "Smart mid-infrared metasurface microspectrometer gas sensing system," Microsyst. Nanoeng. **10**(1), 74 (2024).
14. M. Siemons, M. Hagenaar, A. Adam, *et al.*, "A compressive sensing with photonic crystals enabled spectrometer for trace gas observation," in *International Conference on Space Optics*, vol. 12777 K. Minoglou, N. Karafolas, and B. Cugny, eds., International Society for Optics and Photonics (Proc. SPIE, 2023), p. 127776Y.
15. M. Siemonsa, M. Veen, I. Malysheva, *et al.*, "Development of a photonic crystal spectrometer for greenhouse gas measurements," arXiv (2024).
16. A. Lorente, T. Borsdorff, A. Butz, *et al.*, "Methane retrieved from tropomi: improvement of the data product and validation of the first 2 years of measurements," Atmos. Meas. Tech. **14**(1), 665–684 (2021).
17. S. Guo, F. Wu, S. Albin, *et al.*, "Photonic band gap analysis using finite-difference frequency-domain method," Opt. Express **12**(8), 1741–1746 (2004).
18. V. Liu and S. Fan, "S4 : A free electromagnetic solver for layered periodic structures," Comput. Phys. Commun. **183**(10), 2233–2244 (2012).
19. A. Taflove and S. Hagness, *Computational Electrodynamics: The Finite-Difference Time-Domain Method* (Artech House, 2000), 2nd ed.
20. W. J. Smith, *Modern Optical Engineering: The Design of Optical Systems* (McGraw-Hill Education, 2008), 4th ed.
21. K. Antonov, M. Siemons, X. Van Stein, *et al.*, "Selection of filters for photonic crystal spectrometer using domain-aware evolutionary algorithms," arXiv (2024).
22. M. Siemons and R. Kohlhaas, "Theoretical performance limitations and filter selection based on Fisher information of a computational photonic crystal spectrometer for trace-gas retrieval," *Sensors, Systems, and Next-Generation Satellites XXVIII*, vol. 13192 A. Babu, R. Hélière, and T. Kimura, eds., International Society for Optics and Photonics (,Proc. SPIE, 2024), p. 131920P..
23. D. M. Marques, J. A. Guggenheim, R. Ansari, *et al.*, "Modelling fabry-pérot etalons illuminated by focussed beams," Opt. Express **28**(5), 7691–7706 (2020).
24. K. Varis, M. Mattila, S. Arpiainen, *et al.*, "Reflection of focused beams from opal photonic crystals," Opt. Express **13**(7), 2653–2667 (2005).
25. L. Novotny and B. Hecht, *Principles of Nano-Optics* (Cambridge University Press, 2012).
26. W. Xu, Q. Fan, P. Lin, *et al.*, "Monocrystalline silicon metasurfaces enabled aperture-robust reconstructive spectrometer for visible light," Appl. Phys. Lett. **124**(10), 101702 (2024).
27. M. Born, E. Wolf, B. Bhatia, *et al.*, *Principles of Optics: Electromagnetic Theory of Propagation, Interference and Diffraction of Light* (Cambridge University Press, 1999), 7th ed.
28. J. A. Díaz and R. Navarro, "Geometric optical transfer function and pupil sampling patterns," Optik **279**, 170746 (2023).
29. A. C. Lesina, A. Vaccari, P. Berini, *et al.*, "On the convergence and accuracy of the fdtd method for nanoplasmonics," Opt. Express **23**(8), 10481–10497 (2015).
30. W. yu and R. Mittra, "A conformal finite difference time domain technique for modeling curved dielectric surfaces," IEEE Microw. Wireless Compon. Lett. **11**(1), 25–27 (2001).

Optics EXPRESS

31. Ansys Lumerical, "Understanding mesh refinement and conformal mesh in fdtd," [accessed 22 November 2024], https://optics.ansys.com/hc/en-us/articles/360034382594-Understanding-Mesh-Refinement-and-Conformal-Mesh-in-FDTD.
32. S. S. Panda, H. S. Vyas, and R. S. Hegde, "Robust inverse design of all-dielectric metasurface transmission-mode color filters," Opt. Mater. Express **10**(12), 3145–3159 (2020).
33. Z. Zheng, A. Komar, K. Zangeneh Kamali, *et al.*, "Planar narrow bandpass filter based on si resonant metasurface," J. Appl. Phys. **130**(5), 053105 (2021).
34. S. Wen, X. Xue, S. Wang, *et al.*, "Metasurface array for single-shot spectroscopic ellipsometry," Light: Sci. Appl. **13**(1), 88 (2024).
35. M. Siemons, "Computing focused beam transmissions of photonic crystals using angular spectrum field synthesis dataset," Zenodo (2025), https://doi.org/10.5281/zenodo.14724835.
36. M. Siemons, "pc-field-synthesis," GitHub (2025), https://github.com/MSiemons-SRON/pc-field-synthesis.git, v1.0.